Zhang, W., Chen, W. T., and Williams-Jones, A. E., 2023b, An unique, fluocerite-rich REE deposit in Henan province, Central China: the missing link in magmatic-hydrothermal REE mineralizing systems?: Contributions to Mineralogy and Petrology, v. 178, p. 34

An unique, fluocerite-rich REE deposit in Henan province, Central China: The missing link in magmatic-hydrothermal REE mineralizing systems?

Wei Zhang[1,2], Wei Terry Chen[2,3*], Anthony E. Williams-Jones[4]

1. School of Earth Sciences, Yunnan University, Kunming, 650500, China

2. State Key Laboratory of Ore Deposit Geochemistry, Institute of Geochemistry Chinese Academy of Sciences, Guiyang, 550081, China

3. University of Chinese Academy of Sciences, Beijing, 100049, China

4. Department of Earth and Planetary Sciences, McGill University, Québec H3A OE8, Canada

[*] Corresponding authors: Wei Terry Chen; chenwei@mail.gyig.ac.cn

Abstract

Fluocerite has been shown experimentally and by thermodynamic modelling to be an important phase for the evolution of magmatic-hydrothermal REE mineralizing systems, but one that is rarely observed in nature. The reason for the latter is poorly understood. The newly discovered Taipingzhen REE deposit in Henan province, Central China, is unique for containing abundant fluocerite and thus provides a great opportunity to explore the role of fluocerite in REE mineralization. Fluocerite was the earliest REE mineral to crystallize in this deposit and was replaced extensively by bastnäsite. It has a higher La/Nd ratio than the later-depositing REE minerals, e.g., bastnäsite and monazite. This decrease in the La/Nd ratio with time is interpreted to have resulted from the fluocerite-mediated fractionation of REE (fluocerite prefers the lightestduring its deposition from a high temperature, sulfate-rich hydrothermal fluid, in which the REE were transported as sulfate complexes. This study provides compelling evidence that fluocerite is, indeed, an important, early crystallizing mineral in magmatic-hydrothermal REE systems, that elsewhere was replaced entirely by bastnäsite during subsequent fluid evolution. Moreover, the study shows that the bastnäsite, which replaced fluocerite, inherited its high La/Nd ratio, suggesting that this ratio could be used as a tool with which to identify the former presence of fluocerite. The preservation of fluocerite in the Taipingzhen deposit is interpreted to have been due to the lack of significant cooling until a late stage of mineralization, at which time most of the fluid was lost from the system.

Keywords: Fluocerite paragenesis, Hydrothermal Replacement, Bastnäsite, Fluid Inclusions, REE ore genesis

Introduction

Rare earth elements (REE; Y and 14 elements from La to Lu) are regarded as critical metals as they are indispensable to the development of new and emerging technologies, modern defense systems, and electronic applications. Rare earth element deposits that are genetically associated with carbonatites and/or alkaline silicate rocks are the major providers of REE resources in the world, and thus have long been attractive targets for research and exploration (Weng et al. 2015; Dostal 2016; Verplanck et al. 2016; Simandl and Paradis 2018). Examples include the Bayan Obo and Maoniuping deposits in China, which are the 1st and 3rd largest REE deposits in the World, respectively (Smith and Henderson 2000; Liu et al. 2019).

It is now universally accepted that post-magmatic hydrothermal fluids play an essential role in the formation of carbonatite- and alkaline silicate-related REE deposits (Rankin 2005; Williams-Jones and Palmer 2002; Hou et al. 2009; Trofanenko et al. 2016; Vasyukova and Williams-Jones 2018; Walter et al. 2020). The ore-forming fluids in magmatic-hydrothermal REE deposits (e.g., carbonatite- and alkaline silicate-related REE deposits) are interpreted to be enriched in F, as fluorite and fluorocarbonates (e.g., bastnäsite and parisite) are commonly important minerals in the deposits (e.g., Williams-Jones et al. 2000; Hou et al. 2009; Petrella et al. 2014; Estrade et al. 2015; Zhang et al. 2022). Importantly from the perspective of this study, experimental investigations and thermodynamic modeling predict that, in such F- and REE-enriched hydrothermal fluids, fluocerite [$(Ce,La)F_3$] should precipitate in abundance due to its

low solubility (Migdisov and Williams-Jones 2014; Migdisov et al. 2016). This, however, contrasts with the observation that fluocerite is rarely observed in nature. Indeed, fluocerite has only been reported from a small number of localities, and, until recently, wherever it was discovered it is a minor REE mineral. Examples of such fluocerite occurrences include the Nya Bastnäs Fe–(Cu–) REE deposit in south-central Sweden (Holtstam and Andersson 2007), the Strange Lake REE-Zr-Nb deposit in northeastern Canada (Gysi et al. 2016), and the Baerzhe REE-Nb-Zr-Be deposit in northeastern China (Wu et al. 2021). To resolve the apparent contradiction between the experimental studies and nature, it has been proposed that fluocerite serves as a precursor phase that is subsequently replaced by a more stable REE mineral, such as bastnäsite (Strezlecki et al. 2022).

The newly discovered Taipingzhen REE deposit in Henan province, Central China, in which fluocerite is one of the main REE ore minerals (Qu et al. 2019), requires that we re-evaluate the conclusion of field studies that fluocerite is a relatively unimportant mineral in REE mineralizing natural systems. This deposit also provides an opportunity to test the experimentally rooted hypothesis that fluocerite is an essential precursor for more common REE minerals. In this paper, we report the results of mineralogical, geochemical, and fluid inclusion studies of fluocerite and other REE minerals in the Taipingzhen deposit. The purpose of this study is to interpret the origin of the fluocerite and establish its role in the evolution of this and other REE mineralizing magmatic-hydrothermal systems.

Geological Setting

The orebodies of the Taipingzhen REE deposit are hosted in the Zhangjiazhuang plagiogranite pluton and the volcanic rocks of the Erlangping Group (Fig. 1). The pluton is composed dominantly of plagioclase and quartz accompanied by minor proportions of biotite, hornblende and K-feldspar. Carbonatite dikes 0.2 to 3 m in width crop out to the southeast of the deposit where they intrude the plagio-granite (Fig. 2a). They are composed mainly of calcite (70 vol. %) and contain minor proportions of quartz, apatite, pyrite, barite and fluorite. The REE mineralization of the Taipingzhen deposit is thought to be genetically related to these carbonatites, as the orebodies show a close spatial association with the carbonatites and the latter contain significant proportions of REE minerals, e.g., fluocerite, bastnäsite, parisite and monazite (Zhang et al., 2019). Finally, the plagiogranites that host the orebodies have been strongly fenitized adjacent to their contacts with the carbonatites (Fig. 2a). This alteration is evident from the replacement of the plagioclase by potassium feldspar.

Several ore bodies with a combined total reserve of more than 8 million tons (Mt) of ore grading 2.32 wt. % total REE_2O_3 were identified during geochemical surveys (Li et al. 2017). These ore bodies are subparallel to NWW trending faults and shear zones (Fig. 1). They have a strike extent of up to 2000 m and a thickness of 3 to 10 m (Fig. 2b). The REE mineralization is characterized by abundant hydrothermal veins crosscutting the carbonatites, plagiogranite, and volcanic rocks (Fig. 2b). Based on field observations, two main types of veins have been identified, namely early quartz-calcite-

fluocerite and late quartz-fluorite-bastnäsite veins. The quartz-calcite-fluocerite veins are observed mainly in drill holes at depths > 200 meters (Fig. 2c). They form stockworks (1 to 10 cm in thickness) and are composed of quartz, calcite, barite, fluorite, fluocerite, pyrite, and magnetite. Fluocerite occurs as anhedral to subhedral crystals with diameters varying from 100 to 500 μm (Fig. 3 and Fig. 4). The late quartz-fluorite-bastnäsite veins are widespread and locally crosscut early quartz-calcite-fluocerite veins. They are composed mainly of quartz, calcite, barite, fluorite, bastnäsite and monazite with lesser variable proportions of fluorapatite, pyrite, magnetite, törnebohmite and allanite (Fig. 2d). Bastnäsite and monazite are ubiquitous in the veins and generally are present as euhedral to anhedral crystals with diameters up to several centimeters (Fig. 3e-f).

Methodology

Backscatter electron (BSE) imaging

Backscatter electron (BSE) imaging was conducted on polished thin sections using a JSM-7800F type thermal field scanning electron microscope (SEM) equipped with a TEAM Apollo XL energy dispersive spectrometer and a Mono CL4 cathodoluminoscope at the State Key Laboratory of Ore Deposit Geochemistry (SKLODG), Institute of Geochemistry, Chinese Academy of Sciences, Guiyang, China. Polished thin sections were coated with carbon to avoid electrical charge build-up

during operation. The instruments were operated at an acceleration voltage of 15 kV and a probe current of ~10 nA. Operating conditions (e.g., contrast, brightness) were adjusted during the analyses to ensure that the boundary between the altered and unaltered domains was clearly imaged.

TESCAN Integrated Mineral Analyzer (TIMA) analyses

A mineral map was obtained using a TESCAN Integrated Mineral Analyzer (TIMA) mineralogy system at the SKLODG. The TIMA comprises a TESCAN Mira Schottky field emission scanning electron microscope with four silicon drift energy dispersive (EDS) detectors arranged at 90° intervals around the chamber. The measurements were performed in the dot-mapping mode, and the BSE image was obtained to identify individual particles and boundaries between phases. A rectangular mesh of measurements on every phase was obtained with X-ray spectra. The TIMA measurements were performed at 25 kV using a spot size of ~60 nm and a working distance of 15 mm.

Electron microprobe analysis (EPMA)

Quantitative analyses of the compositions of the REE minerals were carried out at the SKLODG using a JEOL JXA-8530F field emission electron probe microanalyzer. The analyses were performed with a beam spot diameter of 10 μm, a beam current of

10 nA and an acceleration voltage of 25 kV. The analyzing crystals were PETH (K, Th, Ca), LiFH (Pr, Sm), LDE1 (F), and TAP (Na, P, Y), and LIFL (La, Ce, Nd, Gd, Dy, Eu, and Tb). The Kα line was chosen for the measurement of K, Ca, Na, P, F, the Mα line for Th, the Lα line for Y, La, Ce; and the Lβ line for Pr and Sm, Nd, Gd, Dy Eu and Tb. Counting times for the peaks were 10s for K, Na, F, and 30s for the other elements. Background intensity was measured on both sides of the peak with half the counting time for the peak. The standards used for the analyses were orthoclase for K_2O, plagioclase for Na_2O, topaz for F, and monazite for ThO_2, CaO, Pr_2O_3, Sm_2O_3, P_2O_5 Y_2O_3, La_2O_3, Ce_2O_3, Nd_2O_3, Gd_2O_3, Dy_2O_3, Eu_2O_3, Tb_2O_3. The detection limits were approximately 50 to 100 ppm for K and Ca, 100 to 300 ppm for Na, P, and Th, 300-500 ppm for REEs (include Y), and 500 to 700 ppm for F.

Laser Raman spectroscopy

The Raman spectroscopic analysis of fluid inclusions was carried out at the SKLODG, using a LabRAM HR Evolution with an open space microscope equipped with a 20x objective (NA 0.25). The laser spot was 2 μm in diameter. A backscattering geometry was used in the 100-1600 cm^{-1} range, with a 600l.mm^{-1} grating. The Raman spectra were acquired by a 532 nm laser, using a power of ~ 25mW, and two acquisitions that lasted 10 second each. The scanning range for the spectra was set between 100 and 4000 cm^{-1}.

Fluid inclusion microthermometry

Microthermometric measurements of fluid inclusions were conducted on a Linkam THMSG 600 programmable heating-freezing stage mounted on a Leica microscope at the SKLODG. Liquid nitrogen was used to freeze the fluid inclusions. The equipment permits the measurement of phase changes from -196 to 600 °C and was calibrated using the microthermometric behaviour of synthetic fluid inclusions of known composition. For temperatures below 0 °C, the accuracy of the measurements is about ± 0.1 °C and for temperatures above 200 °C, it is about ± 1 °C. A heating rate of 0.1°C/s was used to measure ice and clathrate melting temperatures. The heating rate for measurements of homogenization temperatures was 0.1 to 0.5 °C/s.

Microthermometric data were acquired on fluid inclusion assemblages (Goldstein and Reynolds 1994) in which inclusions in a specific assemblage should display similar phase proportions and microthermometric behavior, if they were trapped coevally. Fluid inclusions were classified as primary, pseudosecondary, and secondary based on the timing of their entrapment relative to the crystallization of the host mineral (Roedder, 1984). The fluid inclusions considered in this study that are either isolated or occur in three-dimensional groups were interpreted to be primary, whereas those aligned along microfractures were designated pseudosecondary or secondary, with the former occupying fractures that terminate within the borders of a crystal. In this study, only primary inclusions showing no evidence of post-entrapment modification were analysed.

Results

Compositions of REE minerals

The fluocerite crystals in the early quartz-calcite-fluocerite veins have commonly been replaced to varying degrees by other REE minerals, notably bastnäsite (Fig. 3a-d). They typically contain a large core of fluocerite surrounded by thin rims of secondary bastnäsite (Fig. 3a-b). In some cases, the primary fluocerite crystals were strongly altered, such that only small relicts (10 to 100 μm) of fluocerite are preserved (Fig. 3c-d). The fluocerite has F and total REE contents varying from 24.6 to 28.9 wt. % and 67.0 to 70.2 wt. %, respectively (Appendix Table 1). Lanthanum and cerium are the main REEs, varying from 22.3 to 34.2 wt. % and 27.1 to 35.3 wt. %, respectively. They are accompanied by subordinate amounts of Pr (1.37 to 2.92 wt. %), and Nd (3.45 to 10.4 wt. %) and trace amounts of Sm (< 0.6 wt. %) and Gd (< 0.3 wt. %). Both fluocerite-(La) and fluocerite-(Ce) are present, but as they may occur irregularly in a single crystal (Appendix Table 1) it is not possible to distinguish them spatially or paragenetically. The La/Nd ratio of the fluocerite varies from 2.14 to 8.73 (Fig. 5a). On a chondrite-normalized REE diagram, the fluocerite is consistently LREE-enriched (Fig. 5b). The bastnäsite (secondary) that replaced fluocerite has La_2O_3, Ce_2O_3, Pr_2O_3, and Nd_2O_3 contents from 26.4 to 33.7 wt. %, 29.8 to 34.1 wt. %, 1.80 to 2.82 wt. %, and 6.37 to 9.96 wt. %, respectively (Appendix Table 1). It has similar La/Nd ratios (2.66

to 5.08) and chondrite-normalized REE profiles to the fluocerite (Fig. 5).

The composition of primary bastnäsite in the late quartz-fluorite-bastnäsite veins differs considerably in composition from the bastnäsite that replaced fluocerite. It is characterized by lower La_2O_3 (21.8 to 24.6 wt. %) and higher Ce_2O_3 (34.3 to 35.8 wt. %), Pr_2O_3 (2.60 to 3.12 wt. %) and Nd_2O_3 (9.80 to 11.7 wt. %) contents (Appendix Table 1). Compared to fluocerite and secondary bastnäsite, it has a lower La/Nd ratio (1.94 to 2.45) and a flatter chondrite-normalized REE profile (Fig. 5).

The monazite crystals have relatively narrow ranges of P_2O_5 (28.0 to 29.8 wt. %) and TREO (68.1 to 71.1 wt. %) contents (Appendix Table 1). The REEs are dominated by La_2O_3 (20.3 to 22.3 wt. %), Ce_2O_3 (32.8 to 34.6 wt. %) and Nd_2O_3 (9.96 to 11.3 wt. %), with subordinate proportions of Pr_2O_3 (2.91 to 3.31 wt. %), Sm_2O_3 (0.45 to 0.86 wt. %) and Gd_2O_3 (0.17 to 0.39 wt. %). The La/Nd ratios and chondrite-normalized REE profiles of the monazite are similar to those of primary bastnäsite (Fig. 5).

Fluid inclusion petrography

Fluid inclusions were observed in quartz from the early quartz-calcite-fluocerite veins and quartz and bastnäsite from the late quartz-fluorite-bastnäsite veins. In both vein-types, the fluid inclusions comprise aqueous-carbonic (AC) and liquid-vapor-solid (LVS) types (Fig. 6).

In the early quartz-calcite-fluocerite veins, the AC inclusions are ellipsoidal or have negative crystal shapes with diameters varying from 10 to 30 μm (Fig. 6a). The

vapor bubble occupies 30 to 50 vol. % of the inclusion. In a very small proportion of AC inclusions, aqueous liquid, carbonic liquid and carbonic vapor are present at ambient temperatures. The LVS inclusions commonly comprise > 70 vol. % of solids (Fig. 6b). They are ellipsoidal or irregular in shape with diameters of up to 50 μm. Most LVS inclusions contain a large isotropic, cubic solid that is interpreted to be halite. In addition to halite, ellipsoidal and spherical solids are observed in some LVS inclusions. It is noteworthy that the AC and LVS inclusions commonly coexist in the early quartz-calcite-fluocerite veins (Fig. 6c).

In the late quartz-fluorite-bastnäsite veins, the AC inclusions are ellipsoidal or have negative crystal shapes with diameters varying from 5 to 20 μm. They typically contain a vapor bubble, occupying 10 to 30 vol. % of the inclusion. The LVS inclusions are distinguishable from those in the early quartz-calcite-fluocerite veins by the smaller proportion and number of solids, one to three (Fig. 6d). As is the case in the early quartz-calcite-fluocerite veins, the main solid is halite and is accompanied by ellipsoidal to spherical solids in some inclusions.

Raman spectroscopic analysis

Raman analyses were performed on vapor phase (bubble) in the AC inclusions and the solids in the LVS inclusions. The bubbles in the AC inclusions produce peaks at 1285 cm^{-1} and 1388 cm^{-1}, indicating that they are composed of CO_2. The ellipsoidal or spherical solids produce Raman peaks at 987, 992, 997, and 1045 cm^{-1} (Fig. 7),

corresponding to aphthitalite ($(K, Na)_3Na(SO_4)_2$), barite ($BaSO_4$), thenardite (Na_2SO_4), and nahcolite ($NaHCO_3$), respectively.

Microthermometry

The carbonic phase of the AC inclusions in both early quartz-calcite-fluocerite veins and late quartz-fluorite-bastnäsite veins crystallized a solid when the temperature was decreased to ~ -100 °C. This solid melted at temperatures of ~ -56 °C (Appendix Table 2), indicating that it is composed dominantly of CO_2. Clathrate formed in the aqueous liquid adjacent to the CO_2 phases and decomposed at a temperature between 3.1 to 5.2 °C in the early veins and from 7.1 to 8.5 °C in the late veins, corresponding to a salinity of 8.66 to 11.75 wt. % NaCl equiv. and 2.96 to 5.51 wt. % NaCl equiv., respectively. The AC inclusions in the early quartz-calcite-fluocerite veins homogenized at temperatures of 358 to 415 °C, which is significantly higher than those in the late quartz-fluorite-bastnäsite veins (175 to 229 °C) (Fig. 8).

The LVS inclusions homogenized to liquid. In the early quartz-calcite-fluocerite veins, the halite dissolved at temperatures varying from 355 to 385 °C and liquid-vapor homogenization occurred to liquid at temperatures between 397 to 448 °C (Appendix Table 2). The other solids generally did not dissolve and are interpreted to be trapped phases. Halite in the LVS inclusions of the late quartz-fluorite-bastnäsite veins dissolved at temperatures of 153 to 193 °C, whereas the liquid and vapor homogenized at temperatures of 218 to 258 °C. The salinity, determined from the dissolution

temperature of the halite (Bodnar and Vityk 1994), was 42.9 to 45.9 wt. % NaCl eq. for the early LVS inclusions, and 29.8 to 31.5 wt. % NaCl eq. for the late LVS inclusions (Appendix Table 2).

Discussion

REE transport and the precipitation of fluocerite

Rare earth elements are transported as aqueous complexes in hydrothermal fluids (Williams-Jones, 2012; Migdisov and Williams-Jones 2014; Migdisov et al. 2016). According to the Hard/Soft Acid/Base principles of Pearson (1963; See also Williams-Jones and Migdisov, 2014), REEs are hard acids (metals) and bond preferentially with hard bases (ligands) such as F^-, SO_4^{2-}, CO_3^{2-}, PO_4^{3-}. Aqueous REE-F complexes are extremely stable (Migdisov et al. 2009), however, the modeling of Migdisov and Williams-Jones (2014) has shown that transport of REEs as fluoride complexes is precluded by the low activity of fluoride ions at low pH due to their association in the weak acid, HF, and the very low solubility of REE-F solids at higher pH. The latter would explain the textural relationships reported earlier showing that fluocerite was the earliest REE mineral to precipitate in the Taipingzhen deposit (Fig. 3 and Fig. 4). Alternative complexes for this deposit, are REE-sulfate complexes, which would be consistent with the common occurrence of sulfate minerals in fluid inclusions (Fig. 6 and Fig. 7) or REE-chloride complexes (chloride is a borderline base and therefore can form stable complexes with both hard and soft acids, Williams-Jones and Migdisov,

2014) which would be favored by the very high salinity of the fluids (see above). In such scenarios, the role of the fluoride ion is that of a binding ligand which promotes REE mineral deposition (Williams-Jones et al., 2012).

Precipitation of fluocerite requires an elevated activity of F^- and REE^{3+} in the fluid and is favored by increasing pH (see above). Thermodynamic modeling and experiments (Migdisov and Williams-Jones, 2014; Strzelechi et al., 2022) have shown that, because of its very low solubility, fluocerite begins precipitating at relatively low pH in REE-enriched fluids (e.g., pH > 3.5 at a temperature of 400 °C), irrespective of whether the REE are transported as sulfate or chloride complexes (Migdisov and Williams-Jones, 2014). Consequently, precipitation of fluocerite is a predicted consequence of the neutralization of acidic fluorine-bearing REE-fertile fluids. The coexistence of AC and LVS inclusions with similar homogenization temperatures in the early quartz-calcite-fluocerite veins indicates phase separation, i.e., the effervescence of an aqueous-carbonic fluid from a high salinity brine (cf. Bowers and Helgeson 1983). This process has the effect of buffering the aqueous fluid to higher pH due to the removal of acidic gases, and we interpret it to be the mechanism that triggered the precipitation of fluocerite in the Taipingzhen deposit.

Replacement of fluocerite by fluid-assisted, coupled dissolution-reprecipitation

Although fluocerite is abundant in the Taipingzhen deposit, pristine, unaltered fluocerite crystals are not observed. Instead, fluocerite has been replaced partially or

wholly by bastnäsite (Fig. 3a-d and Fig. 4). Regardless of the degree of replacement, the altered fluocerite crystals generally preserve their original morphology (pseudomorphism). In addition, pores are observed in the altered domains. These observations indicate that the replacement of fluocerite was driven by fluid-assisted, coupled dissolution-reprecipitation (Putnis 2002, 2009; Putnis and Putnis 2007). This process is driven by the impetus for the system to minimize its Gibbs free energy. Thus, when fluocerite was in the presence of a reactive fluid, it was out of equilibrium and began to dissolve, forming a fluid boundary-layer supersaturated with respect to the more stable secondary phase, bastnäsite. Precipitation of the secondary bastnäsite is interpreted to have occurred on the surface of the fluocerite due to the epitaxial relationship between the fluocerite and the secondary bastnäsite. Because of a higher rate of dissolution than deposition, pores developed, providing pathways for fluid infiltration and promoting replacement (Putnis and Putnis 2007; Ruiz-Agudo et al. 2014).

Fractionation of the REEs during hydrothermal activity

A feature of the chemistry of the REE mineralization in the Taipingzhen deposit is that the chondrite-normalized REE profiles and La/Nd ratios of the REE minerals varied with the evolution of the ore fluids (Fig. 5). This is demonstrated by the fact that the La/Nd ratio of the early fluocerite is much higher than that of the later bastnäsite and monazite. It has also been confirmed by recent experiments showing that LREE-

rich fluocerite is deposited immediately after a REE-bearing solution encounters fluorite, whereas the HREEs travel farther and deposit as HREE-rich fluocerite in the more distal parts of hydrothermal systems (Strzelecki et al. 2022).

The change of the La/Nd ratio from fluocerite to bastnäsite and monazite is interpreted to reflect the fractionation of the REEs during the crystallization of fluocerite. Whether the REE fractionate during REE mineral deposition and the direction of this fractionation (to LREE or HREE) depends on the relative stability and solubility of the various aqueous REE species and the end-member REE solids (Migdisov et al. 2016). The stability of REE chloride complexes decreases strongly from the LREE to the HREE (Migdisov et al., 2009) and that of REE sulfate complexes is independent of the nature of the REE (Migdisov and Williams-Jones, 2008). Consequently, transport of the REE as chloride complexes would favor early deposition of REE minerals with low La/Nd ratios, which is the opposite to what is observed for fluocerite in the Taipingzhen deposit, whereas there would be no effect on the La/Nd ratio of this mineral, if the REE were transported as sulfate complexes. Thermodynamic calculations have shown, however, that the solubility product of fluocerite increases strongly from the LREE to the HREE endmembers (Migdisov et al. 2016). Thus, if the REE were transported as sulfate complexes, this would lead to the observed fractionation of fluocerite from an early variety with a high La/Nd ratio to a later variety with a lower La/Nd ratio, whereas the opposing effects of the stability of the REE chloride complexes and the solubility product for fluocerite would likely lead to no fractionation.

The secondary bastnäsite crystals that replaced fluocerite have REE profiles and La/Nd ratios different from their primary equivalents but similar to those of their precursors (Fig. 5). This indicates that the REE distribution of secondary bastnäsite was inherited from the composition of the fluocerite which it replaced.

The missing link in the formation of magmatic-hydrothermal REE deposits

The results of this study provide the evidence from nature needed to confirm the conclusions reached from experiments and thermodynamic models (Migdisov et al. 2016; Strzelechi et al. 2022) that fluocerite is an important precursor to the formation of magmatic hydrothermal REE deposits, in which bastnäsite is the main ore mineral. In so doing, the study also explains why replacement of fluocerite by bastnäsite is so widespread at Taipingzhen and why such replacement is also a feature of the other occurrences of fluocerite (e.g., Beukes et al. 1991; Holtstam and Andersson 2007; Gysi et al. 2016; Wu et al. 2021). This, in turn, suggests that large-scale fluocerite precipitation is a much more common phenomenon in the formation of REE deposits than previously suspected and that its existence is concealed by the replacement of bastnäsite during the subsequent evolution of the ore-forming hydrothermal system.

Although fluocerite almost invariably is replaced by bastnäsite, the results of our study show that the distribution of the REE in a deposit can continue to record the signature of this important first step in REE ore genesis. This may very well explain why in magmatic-hydrothermal REE deposits, the early precipitated REE minerals (e.g.,

bastnäsite, monazite) generally have significantly higher La/Nd ratios than the later REE minerals, e.g., in the Bayan Obo and Khibina deposits (Zaitsev et al. 1998; Smith et al. 2000). Thus, it is reasonable to propose that the early REE minerals with high La/Nd ratios in these deposits formed by replacing precursory fluocerite.

The Taipingzhen deposit is unique as the only magmatic-hydrothermal REE deposit known to contain abundant fluocerite. A clue to why this is the case is offered by experiments demonstrating that bastnäsite decomposes to REE oxyfluorides and CO_2 at temperatures above ~338°C (Gysi and Williams-Jones 2015). At Taipingzhen, the fluid inclusions in quartz-calcite-fluocerite veins homogenize at temperature > 350 °C, which is significantly higher than in the quartz-bastnäsite-fluorite veins (< 260 °C) (Fig. 8). We, therefore, propose that fluocerite survived alteration to bastnäsite because temperature remained high (above the thermal stability of bastnäsite) until late in the evolution of the hydrothermal system, when there was rapid release of carbonic fluid and a corresponding precipitous drop in temperature (Fig. 9a). As a result, although there was precipitation of abundant late bastnäsite, there was insufficient fluid and time for large-scale replacement of fluocerite by bastnäsite (Fig. 9b). To conclude, the existence of the Taipingzhen fluocerite-dominated REE deposit, provides compelling evidence for the finding from experiments that fluocerite is an important and perhaps essential precursor for the formation of bastnäsite ore deposits.

Concluding Remarks

Fluocerite had been predicted from experiments and thermodynamic considerations to be an early crystallizing REE mineral in fluorine-bearing hydrothermal systems and that it was the precursor to bastnäsite, the main ore mineral in many REE deposits. This has led to the proposal that the replacement of fluocerite by bastnäsite and other fluorcarbonate minerals explains the relatively rare occurrence of this mineral in nature. The discovery of the Taipingzhen deposit, in which fluocerite was a major ore mineral and was both early and replaced by bastnäsite, has confirmed this prediction and proposal. We have provided evidence to show that the abundance of fluocerite at Taipingzhen, which makes this deposit unique, was the result of its formation at unusually high temperature, well above the upper thermal stability of bastnäsite, and the maintenance of this high temperature until a relatively late stage in the hydrothermal system. We have also provided evidence that the REE were transported as sulfate complexes and that, due to the capacity of fluocerite to fractionate the REE (a property not shared by bastnäsite), its composition evolved to progressively lower La/Nd ratios. This characteristic of fluocerite was inherited by the bastnäsite that replaced it, and provides a tool, which we hope researchers will use to test the hypothesis that fluocerite was also an important precursor mineral in other fluorcarbonate REE deposits where it is no longer present.

Acknowledgements

This study was supported by the National Natural Science Foundation of China (42103065, 42121003, 92162323). We are grateful to Xiang Li, Shao-Hua Dong and

Chao Wang for their kind support of analyses. The assistance of Hua-Kai Chen and Jing-Hui Li of the Nuclear Geological Bureau in the fieldwork is also gratefully acknowledged. This manuscript was improved significantly by the insightful comments of Associate editor, Dante Canil and those of Wyatt Bain and an anonymous referee.

References

Bayliss P, Levinson AA (1988) A system of nomenclature for rare earth mineral species: Revision and extension. American Mineralogist 73: 422–423.

Beukes GJ, De Bruiyn H, Van Der Westhuizen WA (1991) Fluocerite and associated minerals from the Baviaanskranz granite pegmatite near Kakamas, South Africa. South African Journal of Geology 94: 313-320.

Bodnar RJ, Vityk MO (1994) Interpretation of microthermometric data for H2O-NaCl fluid inclusions. In: Vivo De B, Frezzotti ML, eds Fluid inclusions in minerals, Methods and Applications. Virginia Tech, Blacksburg: 117-130.

Bowers TS, Helgeson HC (1983) Calculation of the thermodynamic and geochemical consequences of nonideal mixing in the system H_2O-CO_2-NaCl on phase relations in geologic systems: metamorphic equilibria at high pressures and temperatures. American Mineralogist 68: 1059-1075.

Dostal J (2016) Rare metal deposits associated with alkaline/peralkaline igneous rocks. in Verplanck P. L., and Hitzman M. W., eds., Rare earth and critical elements in ore deposits. Society of Economic Geologists 18: 33-54.

Estrade G, Salvi S, Béziat D, Williams-jones AE (2015) The origin of skarn-hosted rare-metal mineralization in the Ambohimirahavavy alkaline complex, Madagascar. Economic Geology 110: 1485-1513.

Goldstein RH, Reynolds TJ (1994) Systematics of fluid inclusions in diagenetic minerals. Society of Sedimentary Geology, SEPM Short Course 31, 199p.

Gysi AP, Williams-Jones AE (2015) The thermodynamic properties of bastnäsite-(Ce) and parisite-(Ce). Chemical Geology 392: 87-101.

Gysi AP, Williams-Jones AE, Collins P (2016) Lithogeochemical Vectors for Hydrothermal Processes in the Strange Lake Peralkaline Granitic REE-Zr-Nb Deposit. Economic geology 111: 1241-1276.

Haas JR, Shock EL, Sassani DC (1995) Rare earth elements in hydrothermal systems: Estimates of

standard partial molal thermodynamic properties of aqueous complexes of the rare earth elements at high pressure and temperatures. Geochimica Et Cosmochimica Acta 59: 4329-4350.

Holtstam D, Andersson UB (2007) The REE minerals of the Bastnäs-type deposits, South-central Sweden. The Canadian Mineralogist 45: 1073-1114.

Hou ZQ, Tian SH, Xie YL, Yang ZS, Yuan ZX, Yin SP, Yi LS, Fei HC, Zou TR, Ge B (2009) The Himalayan Mianning–Dechang REE belt associated with carbonatite–alkaline complexes, eastern Indo-Asian collision zone, SW China. Ore Geology Reviews, 36 65-89.

Li J, Chen H, Zhang H, Zhang Y, Zhang T, Wen G, Zhang P (2017) Mineralization characteristics and ore genesis of the light rare earth deposit in Taiping Town, western Henan. Geology in China 44: 288-300 (in Chinese with English abstract).

Liu Y, Chakhmouradian AR, Hou ZQ, Song W, Kynicky J (2019) Development of REE mineralization in the giant Maoniuping deposit (Sichuan, China): insights from mineralogy, fluid inclusions, and trace-element geochemistry. Mineralium Deposita 5: 701-718.

Migdisov AA, Williams-Jones AE (2014) Hydrothermal transport and deposition of the rare earth elements by fluorine-bearing aqueous liquids. Mineralium Deposita 49: 987-997.

Migdisov A, Williams-Jones AE, Brugger J, Caporuscio FA (2016) Hydrothermal transport, deposition, and fractionation of the REE: Experimental data and thermodynamic calculations. Chemical Geology 439: 13-42.

Migdisov AA, Williams-Jones AE, Wagner T (2009) An experimental study of the solubility and speciation of the rare earth elements (III) in fluoride- and chloride-bearing aqueous solutions at temperatures up to 300 ° C. Geochimica Et Cosmochimica Acta 73: 7087-7109.

Pearson RG (1963) Hard and soft acids and their bases. Journal Of The American Chemical Society 110: 7684-7690.

Petrella L, Williams-Jones AE, Goutier J, and Walsh J (2014) The Nature and Origin of the Rare Earth Element Mineralization in the Misery Syenitic Intrusion, Northern Quebec, Canada. Economic Geology 109: 1643-1666.

Putnis A (2002) Mineral replacement reactions: from macroscopic observations to microscopic mechanisms. Minerlogical Magazine 66: 689-708.

Putnis A (2009) Mineral replacement reactions. Thermodynamics and kinetics of water-rock

interaction. In: Oelkers EH, Schott J (eds) Reviews in mineralogy and geochemistry 70: 87–124.

Putnis A, Putnis CV (2007) The mechanism of reequilibration of solids in the presence of a fluid phase. Journal of Solid State Chemistry 180: 1783-1786.

Qu K, Sima X, Li G, Fan G, Li T, Guo H, Yin Q, Li J (2019) Mineralogical study of the fluocerite-(La) found firstly in China. Bulletin of Mineralogy, Petrology and Geochemistry 38: 764-772 (in Chinese with English abstract).

Rankin AH (2005) Carbonatite-associated rare metal deposits: composition and evolution of ore-forming fluids-the fluid inclusion evidence. Geological Association of Canada, Short Course Notes 17: 299-314.

Roedder E 1984, Fluid inclusions. Reviews in Mineralogy, 12, 644 p.

Ruiz-Agudo E, Putnis CV, Putnis A (2014) Coupled dissolution and precipitation at mineral-fluid interfaces. Chemical Geology 383: 132-146.

Simandl GJ, Paradis S (2018) Carbonatites: related ore deposits, resources, footprint, and exploration methods. Applied Earth Science 4: 123-152.

Smith MP, Henderson P (2000) Preliminary fluid inclusion constraints on fluid evolution in the Bayan Obo Fe-REE-Nb deposit, Inner Mongolia, China. Economic Geology, 95: 1371-1388.

Smith MP, Henderson P, Campbell LS (2000) Fractionation of the REE during hydrothermal processes: constraints from the Bayan Obo Fe-REE-Nb deposit, Inner Mongolia, China. Geochimica et Cosmochimica Acta, 64: 3141-3160.

Strzelechi AC, Migdisov A, Boukhalfa H, Sauer K, Mclntosh KG, Currier RP, Williams-Jones AE, Guo XF (2022) Fluocerite as a precursor to rare earth element fractionation in ore-forming systems. Nature Geoscience, 15: 327-333.

Trofanenko J, Williams-Jones AE, Simandl GJ, Migdisov AA (2016) The nature and origin of the REE mineralization in the Wicheeda carbonatite, British Columbia, Canada. Economic geology, 111: 199-223.

Vasyukova OV, Williams-Jones AE (2018) Direct measurement of metal concentrations in fluid inclusions, a tale of hydrothermal alteration and REE ore formation from Strange Lake, Canada. Chemical Geology, 483: 285-396.

Verplanck PL, Mariano AN, Mariano AJ (2016) Rare earth element ore geology of carbonatites. in: Verplanck P L and Hitzman M W, eds. Rare earth and critical elements in ore deposits. Reviews in Econ. Geol. 18: 5-32.

Walter BF, Steele-Macinnis M, Giebel RJ, Marks MAW, Markl G (2020) Complex carbonate-sulfate brines in fluid inclusions from carbonatites: Estimating compositions in the system H_2O-Na-K-CO_3-SO_4-Cl. Geochim Cosmochim Ac 277: 224-242.

Weng Z, Jowitt SM, Mudd GM, Haque N (2015) A detailed assessment of global rare earth element resources: Opportunities and challenges. Economic Geology 110: 1925-1952.

Williams-Jones AE, Palmer DAS (2002) The evolution of aqueous-carbonic fluids in the Amba Dongar barbonatite, India: implications for fenitisation. Chem Geol 185: 283-301.

Williams-Jones AE, Samson IM, Olivo GR (2000) The genesis of hydrothermal fluorite-REE deposits in the Gallinas Mountains, New Mexico. Economic Geology 95: 327-342.

Wood SA (1990) The aqueous geochemistry of the rare earth elements and yttrium: 1. Review of available low-temperature data for inorganic complexes and the inorganic REE speciation of natural waters. Chemical Geology 82: 159-186.

Wu M, Samson IM, Qiu K, Zhang D (2021) Concentration mechanisms of rare earth element-Nb-Zr-Be mineralization in the Baerzhe deposit, Northeast China: Insights from textural and chemical features of amphibole and rare metal minerals. Economic Geology, 116.

Zaitsev AN, Wall F, Le Bas MI (1998) REE-Sr-Ba minerals from the Khibina carbonatites, Kola Peninsula, Russia: Their mineralogy, paragenesis and evolution. Mineralogical Magazine 62: 225-250.

Zhang W, Chen WT, Mernagh TP, Zhou L (2022) Quantifying the nature of ore-forming fluids in the Dalucao carbonatite-related REE deposit, Southwest China: implication for the transport and deposition of REEs. Mineralium Deposita 57: 935-953.

Figure captions

Fig. 1 A geological map of the Taipingzhen REE deposit (modified from Li et al., 2017).

Fig. 2 Photographs of carbonatites and REE ores in the Taipingzhen REE deposit. (a) Carbonatite dike intruding the plagio-granite with intensive fenitization at the contact zone; (b) High-grade hydrothermal veins crosscutting the plagio-granite; (c) Early quartz-calcite-fluocerite veins in the drill holes; (d) Late quartz-fluorite-bastnäsite veins containing abundant bastnäsite grains. Abbreviations: Cal = calcite, Fcrt = fluocerite, Py = pyrite, Bsn = bastnäsite, Fl = fluorite.

Fig. 3 Backscattered electron (BSE) images showing the occurrence of REE minerals in the Taipingzhen REE deposit. (a-b) Slightly altered fluocerite crystals containing large cores surrounded by secondary bastnäsite. (c-d) Relict fluocerite in a matrix of secondary bastnäsite. (e) An intergrowth of euhedral bastnäsite with quartz and fluorite; (f) A large euhedral monazite crystal intergrown with bastnäsite. Abbreviations: Qtz = quartz, Syn = synchysite, Mnz = monazite.

Fig. 4 (a) TESCAN Integrated Mineral Analyzer (TIMA) map showing the alteration of fluocerite in the Taipingzhen deposit. (b) A partially altered crystal with a large core of fluocerite. (c) Highly altered crystals containing relicts of fluocerite.

Fig. 5 (a) Box and whisker plots showing the variation of La/Nd ratios in fluocerite, bastnäsite and monazite. (b) Chondrite-normalized REE profiles for fluocerite, bastnäsite, and monazite (average value).

Fig. 6 Photomicrographs of fluid inclusions in the Taipingzhen deposit. (a) Negative crystal-shaped aqueous-carbonic (AC) inclusions in the quartz of early quartz-calcite-fluocerite veins. (b) A liquid-vapor-solid (LVS) inclusion with halite and aphthitalite crystals in the fluorite of early quartz-calcite-fluocerite veins. (c) Coexistence of aqueous-carbonic (AC) and liquid-vapor-solid (LVS) inclusions in the fluorite of early quartz-calcite-fluocerite veins. (d) A liquid-vapor-solid (LVS) inclusion with a halite crystal in the quartz of late quartz-fluorite-bastnäsite veins.

Fig. 7 Laser Raman spectra of aphthitalite (a), barite (b), thenardite (c) and nahcolite (d) solids in the LVS inclusions of early quartz-calcite-fluocerite veins.

Fig. 8 Histograms showing the final homogenization temperatures of fluid inclusions in early quartz-calcite-fluocerite and late quartz-fluorite-bastnäsite veins.

Fig. 9 A cartoon illustrating the crystallization and replacement of fluocerite in the Taipingzhen deposit (a) Early crystallization of fluocerite as a result of carbonic phase separation. (b) Later crystallization of bastnäsite and monazite, and the pervasive replacement of fluocerite by bastnäsite.

Fig. 1 A geological map of the Taipingzhen REE deposit (modified from Li et al., 2017).

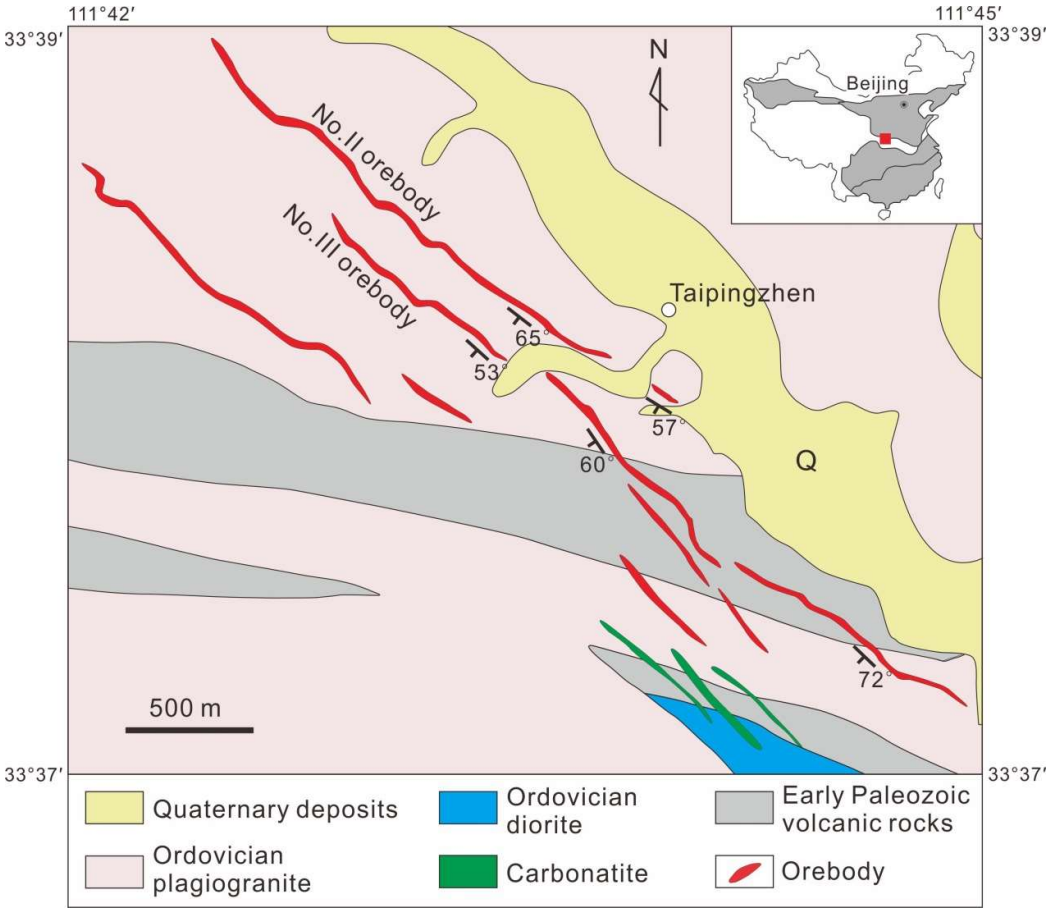

Fig.2 Photographs of carbonatites and REE ores in the Taipingzhen REE deposit. (a) A carbonatite dike in the plagiogranite displaying evidence of intense fenitization adjacent to its contact with the latter; (b) High-grade hydrothermal veins crosscutting the plagiogranite; (c) Early quartz-calcite-fluocerite veins in drill core; (d) Late quartz-fluorite-bastnäsite veins containing numerous bastnäsite crystals. Abbreviations: Cal = calcite, Fcrt = fluocerite, Py = pyrite, Bsn = bastnäsite, Fl = fluorite.

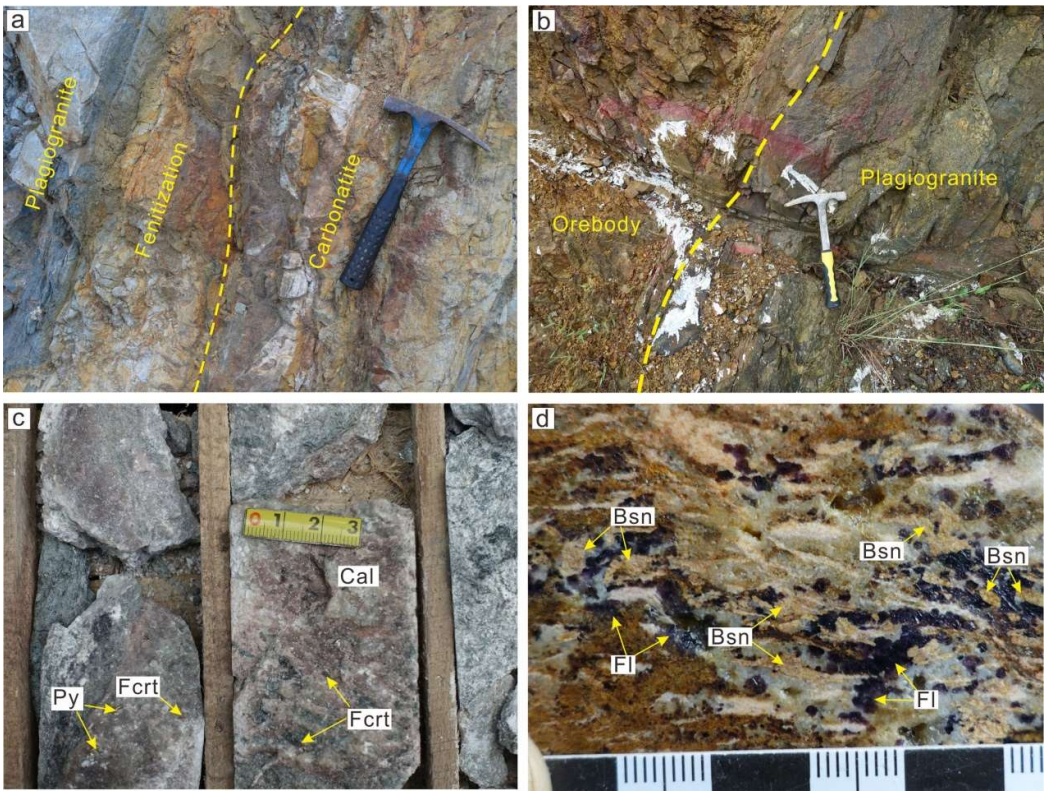

Fig. 3 Backscattered electron (BSE) images showing the occurrence of REE minerals in the Taipingzhen REE deposit. (a-b) Slightly altered fluocerite crystals containing large cores surrounded by secondary bastnäsite. (c-d) Relict fluocerite in a matrix of secondary bastnäsite. (e) An intergrowth of euhedral bastnäsite with quartz and fluorite; (f) A large euhedral monazite crystal intergrown with bastnäsite. Abbreviations: Qtz = quartz, Syn = synchysite, Mnz = monazite.

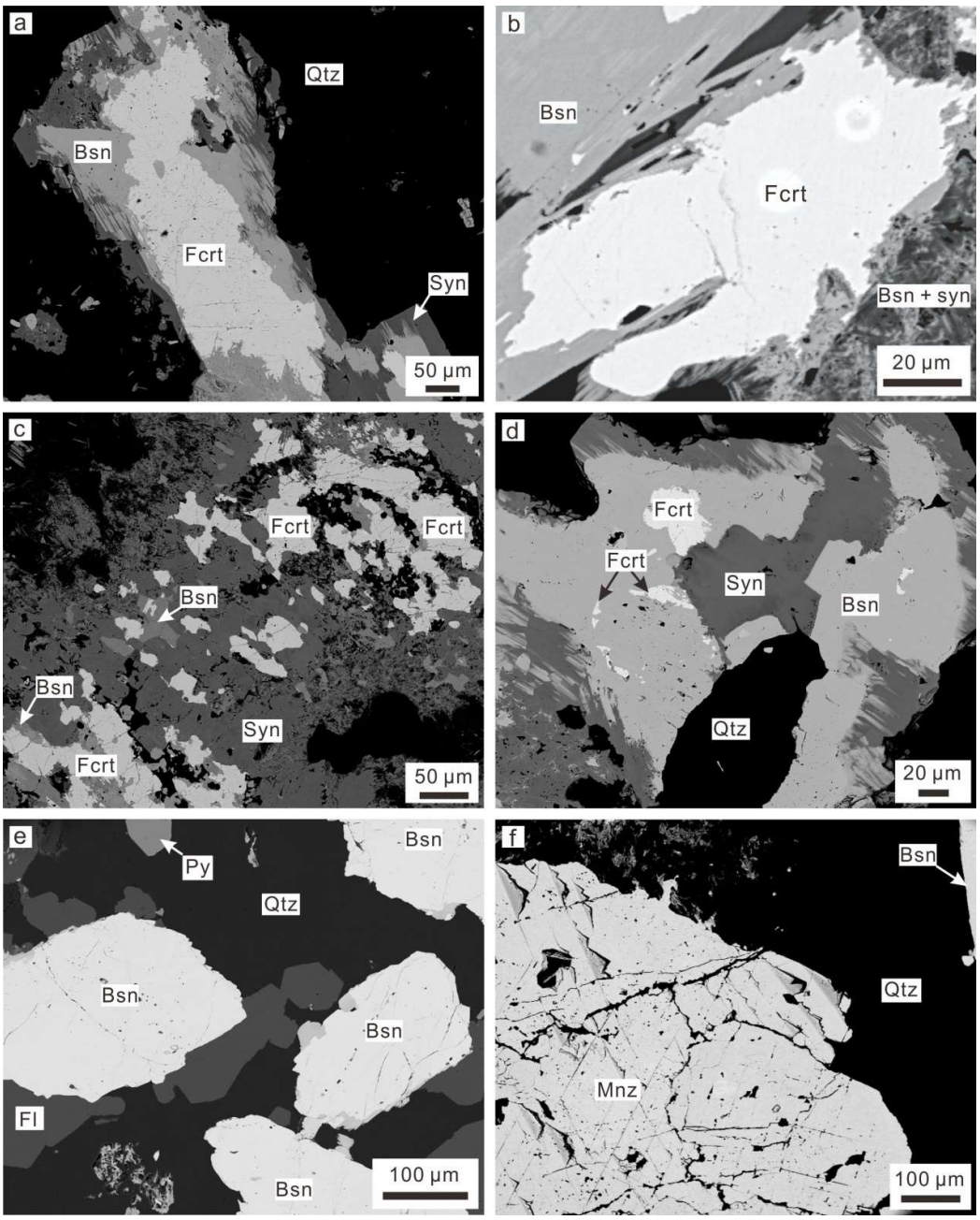

Fig. 4 (a) TESCAN Integrated Mineral Analyzer (TIMA) map showing the alteration of fluocerite in the Taipingzhen deposit. (b) A partially altered crystal with a large core of fluocerite. (c) Highly altered crystals containing relicts of fluocerite.

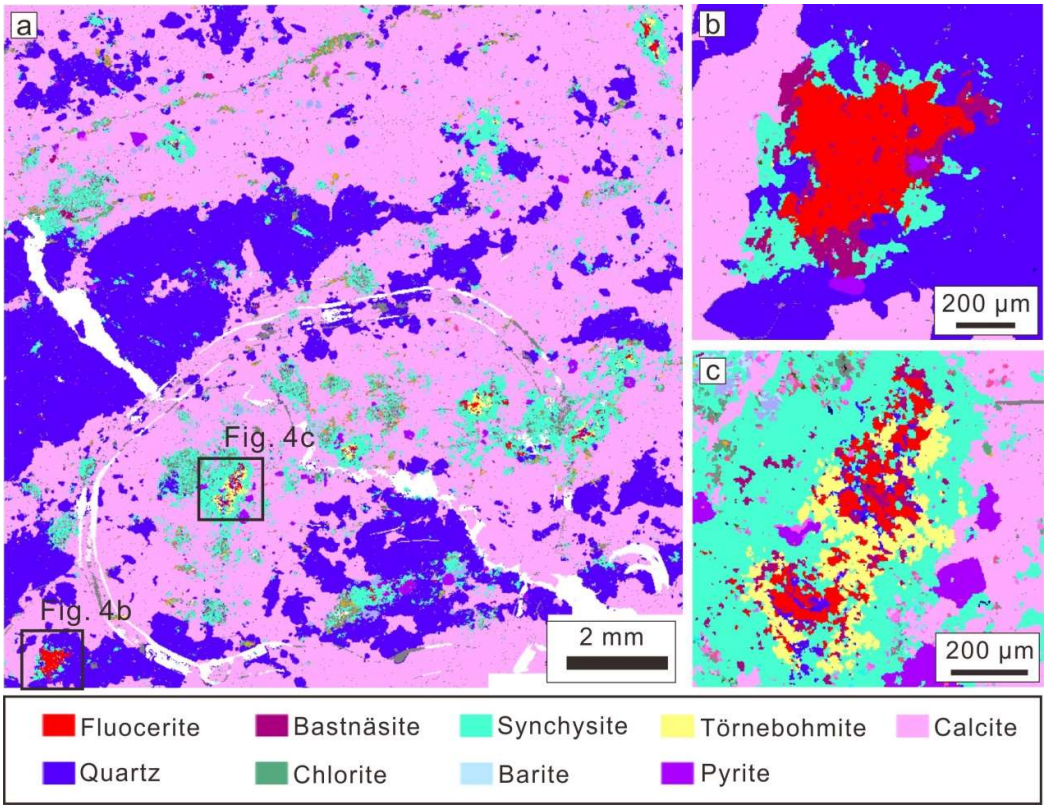

Fig. 5 (a) Box and whisker plots showing the variation of La/Nd ratios in fluocerite, bastnäsite and monazite. (b) Chondrite-normalized REE profiles for fluocerite, bastnäsite, and monazite (average value).

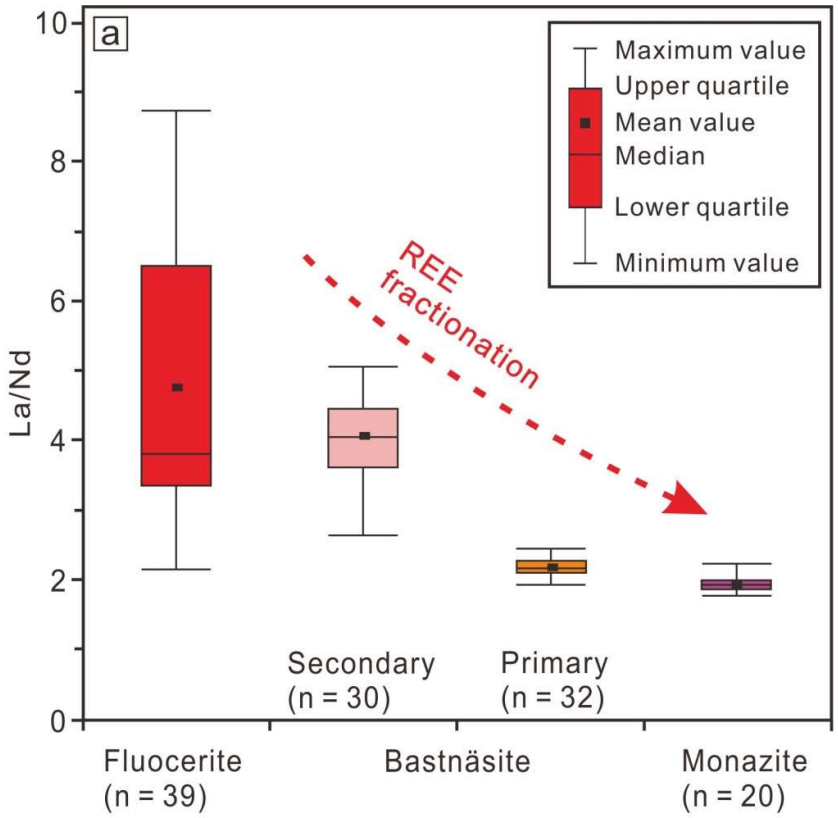

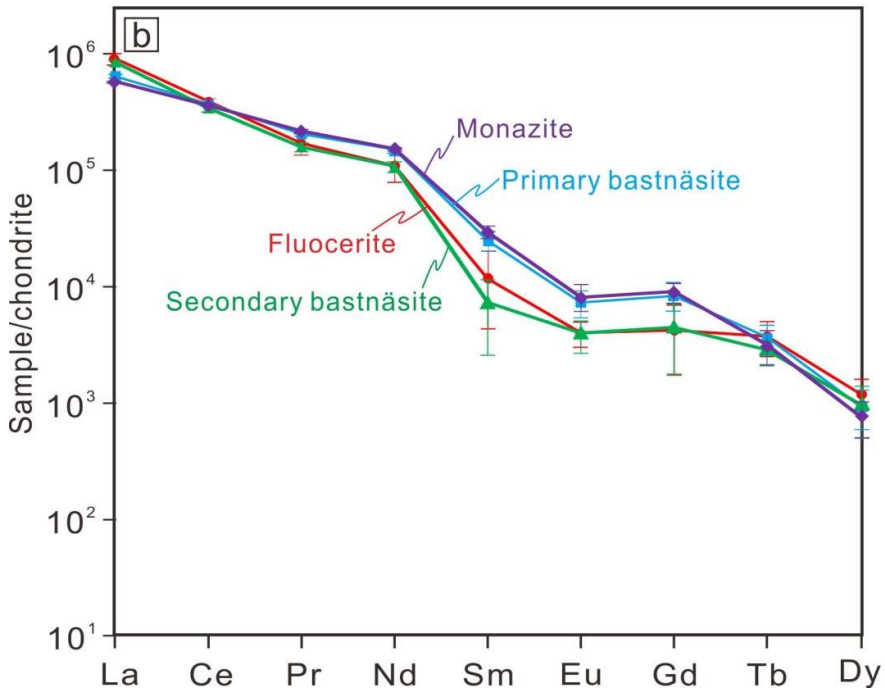

Fig. 6 Photomicrographs of fluid inclusions in the Taipingzhen deposit. (a) Negative crystal-shaped aqueous-carbonic (AC) inclusions in the quartz of early quartz-calcite-fluocerite veins. (b) A liquid-vapor-solid (LVS) inclusion with halite and aphthitalite crystals in the fluorite of early quartz-calcite-fluocerite veins. (c) Coexistence of aqueous-carbonic (AC) and liquid-vapor-solid (LVS) inclusions in the fluorite of early quartz-calcite-fluocerite veins. (d) A liquid-vapor-solid (LVS) inclusion with a halite crystal in the quartz of late quartz-fluorite-bastnäsite veins.

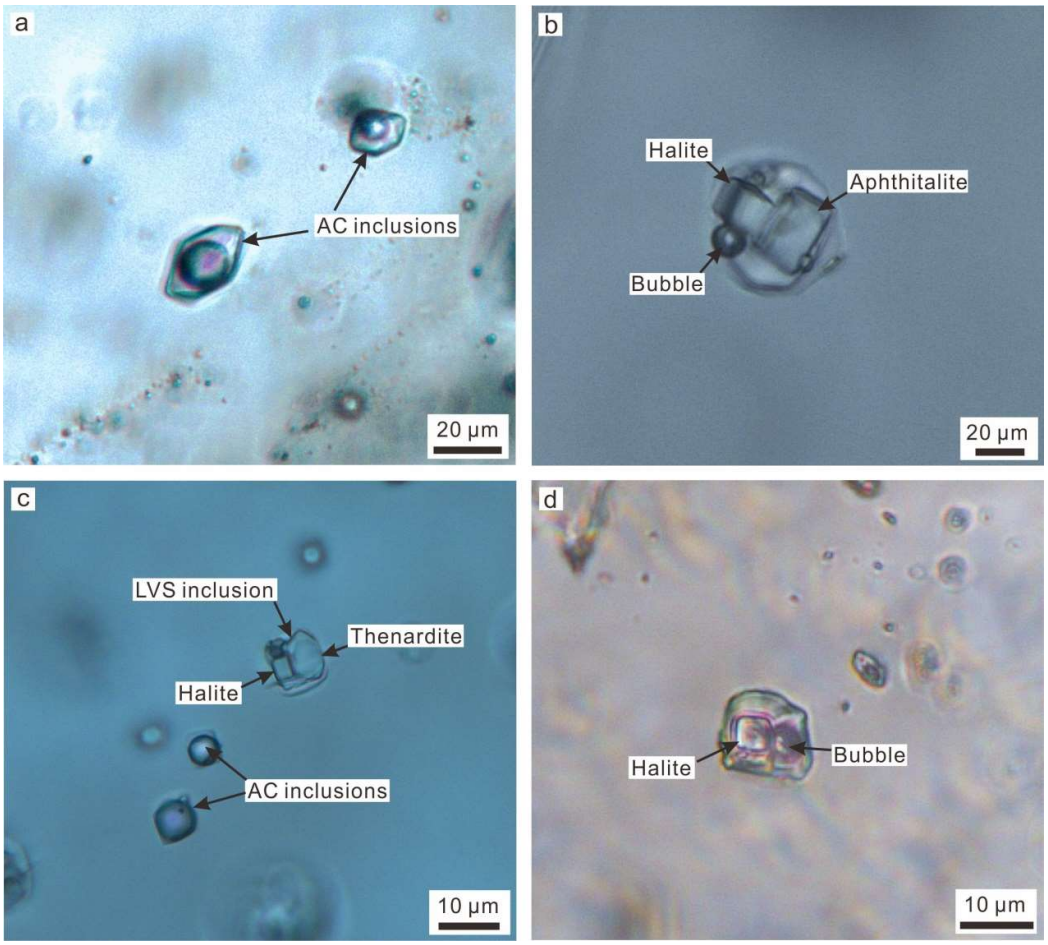

Fig. 7 Laser Raman spectra of aphthitalite (a), barite (b), thenardite (c) and nahcolite (d) in the LVS inclusions of early quartz-calcite-fluocerite veins.

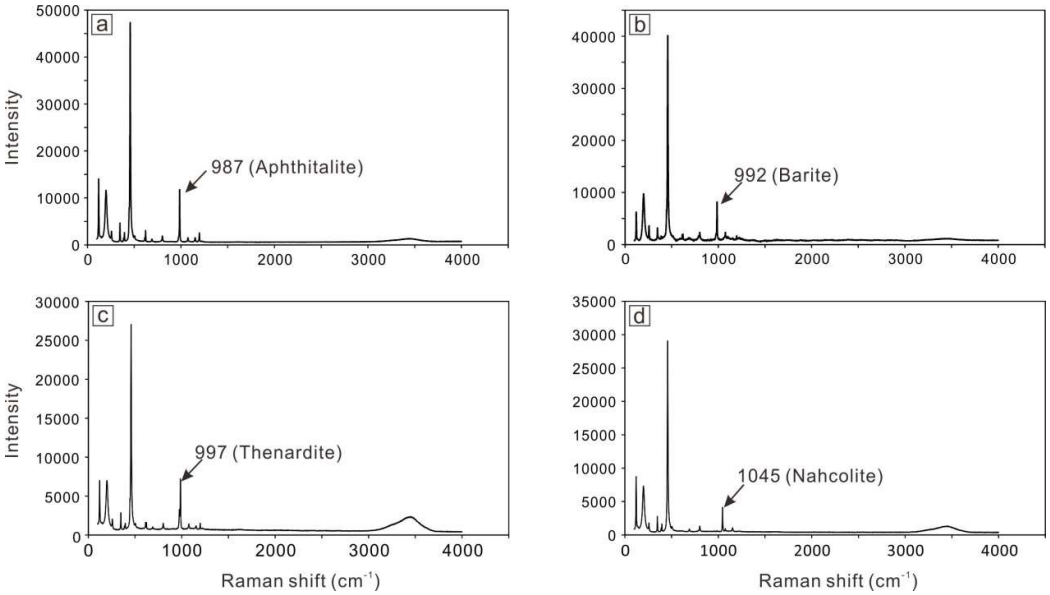

Fig. 8 Histograms showing the mean final homogenization temperatures of fluid inclusion assemblage in early quartz-calcite-fluocerite and late quartz-fluorite-bastnäsite veins.

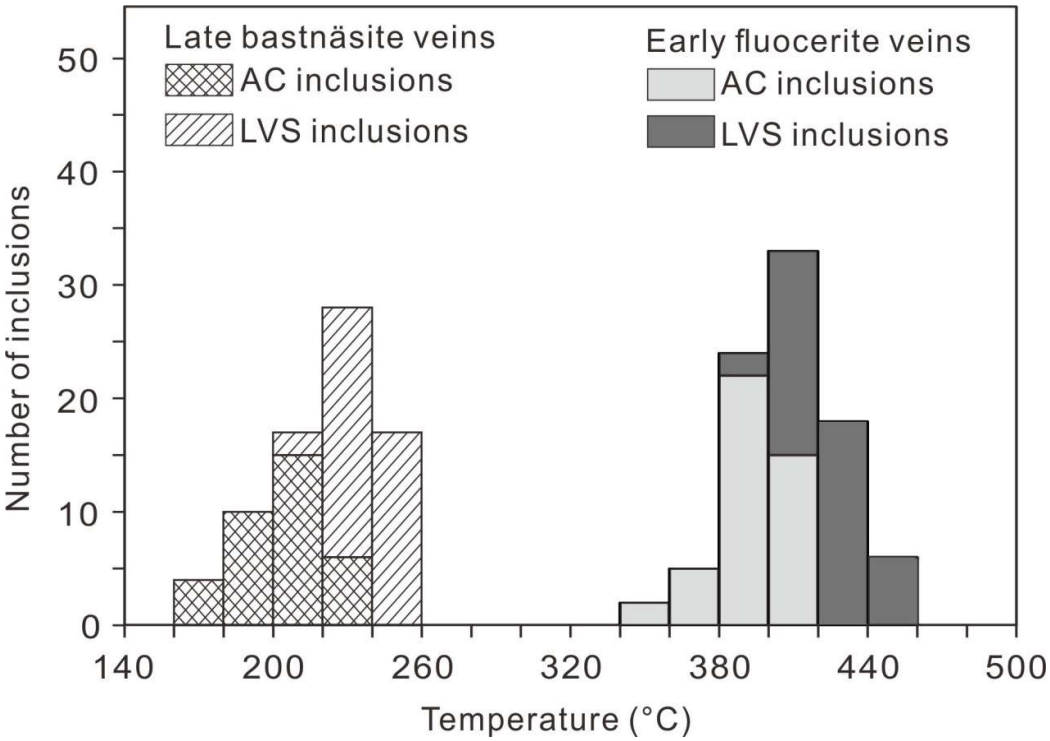

Fig. 9 A cartoon illustrating the crystallization and replacement of fluocerite in the Taipingzhen deposit (a) Early crystallization of fluocerite as a result of carbonic phase separation. (b) Later crystallization of bastnäsite and monazite, and the pervasive replacement of fluocerite by bastnäsite.